

See discussions, stats, and author profiles for this publication at: <https://www.researchgate.net/publication/243374369>

# Hydrogen Absorption and Diffusion in Bulk $\alpha$ -MoO<sub>3</sub>

ARTICLE in THE JOURNAL OF PHYSICAL CHEMISTRY C · JULY 2009

Impact Factor: 4.77 · DOI: 10.1021/jp9017212

CITATIONS

37

READS

56

## 5 AUTHORS, INCLUDING:



**Xianwei Sha**

Engility Corporation

43 PUBLICATIONS 1,180 CITATIONS

SEE PROFILE



**Liang Chen**

National University of Defense Technology

109 PUBLICATIONS 1,339 CITATIONS

SEE PROFILE



**Alan C. Cooper**

Air Products and Chemicals

44 PUBLICATIONS 1,213 CITATIONS

SEE PROFILE



**Hansong Cheng**

China University of Geosciences

165 PUBLICATIONS 2,355 CITATIONS

SEE PROFILE

# Hydrogen Absorption and Diffusion in Bulk $\alpha$ -MoO<sub>3</sub>

Xianwei Sha,<sup>†</sup> Liang Chen,<sup>‡</sup> Alan C. Cooper,<sup>†</sup> Guido P. Pez,<sup>†</sup> and Hansong Cheng<sup>\*,†</sup>

Air Products and Chemicals, Inc., 7201 Hamilton Boulevard, Allentown, Pennsylvania 18195-1501, and Ningbo Institute of Materials Technology and Engineering, Chinese Academy of Sciences, Ningbo, Zhejiang 315201, People's Republic of China

Received: February 24, 2009; Revised Manuscript Received: April 1, 2009

The absorption, diffusion, and desorption of atomic hydrogen in layered orthorhombic molybdenum trioxide ( $\alpha$ -MoO<sub>3</sub>) was investigated using density functional theory. Hydrogen atoms are absorbed in bulk  $\alpha$ -MoO<sub>3</sub> to form the hydrogen molybdenum bronze H<sub>x</sub>MoO<sub>3</sub> ( $x = 0.25, 0.5, 0.75, 1, 1.25, \text{ and } 1.5$ ). The semiconductor band gap of bulk  $\alpha$ -MoO<sub>3</sub> shifts to metallic upon hydrogen bronze formation at the H atom loadings selected in the present study. The hydrogen atoms become protonic when coordinated to oxygen, which gives rise to a charge reduction on the Mo atoms adjacent to the absorption sites. Hydrogen migration along a prescribed diffusion pathway in the lattice was found to be facile due to small energy barriers for H atom transfer between O atoms, facilitated by a hydrogen bonding network. The sequential hydrogen desorption from the bronze and the mechanisms of hydrogen spillover in  $\alpha$ -MoO<sub>3</sub> are also discussed.

## I. Introduction

The phenomenon known as hydrogen spillover has recently drawn substantial experimental and theoretical attention as an important technique for the storage of hydrogen at high densities under near-ambient conditions in lightweight solid-state materials.<sup>1</sup> This phenomenon has been studied for more than 40 years using a number of transition metal oxides.<sup>2</sup> Recent studies pioneered by Yang and co-workers have demonstrated that hydrogen spillover also occurs with a variety of carbon-based materials.<sup>3–6</sup> Unusually high hydrogen storage capacities under near-ambient conditions were achieved via hydrogen spillover with several materials including metal-organic frameworks and low-silica type X zeolites. Increases of hydrogen storage capacity by a factor of 2.9 in activated carbon and a factor of 1.6 in single-walled carbon nanotubes via hydrogen spillover have been reported.<sup>3</sup> The effects of hydrogen spillover have been further independently demonstrated in several recent experiments using transition metal oxides and carbon-based materials.<sup>7–11</sup> The stored hydrogen atoms in the carbon-based materials were found to be loosely adsorbed on the substrate surfaces upon H<sub>2</sub> dissociation using a catalyst,<sup>12</sup> and metal doping of the substrate was reported to significantly enhance hydrogen spillover and storage.<sup>13</sup> Mitchell et al. investigated hydrogen spillover on carbon-supported precious metal catalysts using inelastic neutron scattering spectroscopy and identified two different forms of absorbed hydrogen: H at edge sites of graphite layers and a weakly bound layer of mobile H atoms.<sup>14</sup> The proposed hydrogen spillover mechanism can be briefly summarized as follows.<sup>4,5</sup> Hydrogen molecules in the gas phase interact with a transition metal catalyst and dissociate on the catalyst surface. The generated H atoms then migrate from the catalyst particles to the substrate/storage material and diffuse throughout the entire bulk solid. The key to the occurrence of hydrogen spillover in solid state materials is the high mobility of the generated H atoms, which should be able to move freely at near-ambient temperatures from the vicinity of the catalyst particles to sites

on the substrate far from where the catalyst particles reside. While active research efforts have been directed toward understanding the hydrogen spillover process on carbon-based hydrogen storage compounds,<sup>15–17</sup> there has been no general consensus of how to explain the observed large reversible hydrogen storage capacity and facile desorption kinetics via a reverse of the spillover.<sup>18</sup>

Despite much debate about the spillover processes in carbon-based materials, hydrogen spillover is a widely accepted experimental phenomenon for many metal oxides<sup>19–21</sup> and sulfides.<sup>22,23</sup> A significant improvement of hydrogen spillover efficiency on metal oxides can be made via addition of metal catalysts.<sup>2</sup> Smith and Rohrer used atomic force microscopy and X-ray diffraction to characterize the structural evolution of a MoO<sub>3</sub> (010) surface during the gas-phase reaction with hydrogen. They demonstrated that MoO<sub>3</sub> intercalates H atoms which results in protonation and precipitation of hydrogen molybdenum bronze.<sup>24,25</sup> Noh et al. reported that H atoms are highly mobile within MoO<sub>3</sub> and the formation of hydrogen bronze is an extremely fast process.<sup>21</sup> To examine the bonding properties, location, and mobility of hydrogen in H<sub>x</sub>MoO<sub>3</sub>, Ritter and co-workers performed solid-state <sup>1</sup>H nuclear magnetic resonance (NMR) spectroscopy studies and reported that H atoms preferentially occupy the intralayer positions on a quasi-one-dimensional zigzag line connecting the vertex-sharing oxygen atoms of the MoO<sub>6</sub> octahedra. After saturation of these sites, the hydrogen populates interlayer positions coordinated with terminal oxygen atoms. The activation energies of hydrogen diffusion were found to be on the order of 15–30 kJ/mol.<sup>26–28</sup> Several experimental studies demonstrated that the semiconducting transition metal oxide compounds, predominantly tungsten and/or molybdenum oxides, become metallic immediately upon hydrogen bronze formation via spillover,<sup>21,29,30</sup> but the mechanism of transition is yet to be fully understood. Dutta et al. recently reported an increase in hydrogen storage capacity via spillover on CeO<sub>2</sub> at the presence of Pt catalysts, and their NMR studies indicated the presence of protonic hydrogen over the catalyst surfaces.<sup>7</sup> Mechanistic understanding of these well-known hydrogen spillover processes in metal

\* Corresponding author. E-mail: chengh@airproducts.com.

<sup>†</sup> Air Products and Chemicals, Inc.

<sup>‡</sup> Chinese Academy of Sciences.

oxides should shed light on spillover in carbon-based materials. In a recent communication, we reported density functional studies of hydrogen spillover on the  $\text{MoO}_3(010)$  surface.<sup>31</sup> The platinum catalyst was modeled with a small Pt cluster, and its catalytic activity was examined at the limit of full saturation of H atoms to account for the constant  $\text{H}_2$  pressure maintained in experiments.<sup>32</sup> Subsequently, the energetic profiles associated with hydrogen atom migration from the catalyst to the substrates and hydrogen diffusion on the substrates were mapped out by calculating minimum energy pathways. We found that hydrogen spillover in the transition metal oxide is governed by the massive hydrogen bonding networks inherent in the metal oxide lattice.

Most of the theoretical studies to date have focused on H adsorption and diffusion on  $\text{MoO}_3$  surfaces,<sup>31,33–39</sup> and very little effort has been made to study absorption and diffusion of H in the bulk, which is critical for understanding the formation of  $\text{H}_x\text{MoO}_3$  bronze precipitates and the observed high hydrogen density of the hydrogen bronzes. In this report, we attempt to address the mechanisms of hydrogen spillover in bulk  $\text{MoO}_3$  by performing first-principles calculations using density functional theory. The relative absorption strengths and diffusivities of H atoms in the lattice are studied by performing full structural optimizations and computing minimum energy pathways. The mechanism of transition from semiconducting  $\text{MoO}_3$  to metallic bronze materials upon hydrogen spillover is examined by calculating the electronic structures of these compounds. We also investigate the influence of hydrogen concentrations in the lattice on the physicochemical properties of  $\text{MoO}_3$ .

## II. Computational Methods

All of the first-principles calculations were performed using density functional theory (DFT) with a periodic boundary condition as implemented in the Vienna ab initio simulation package (VASP).<sup>40,41</sup> The Kohn–Sham equation was solved iteratively using a plane wave basis set with a cutoff energy of 400 eV to describe the valence electrons. The exchange–correlation effects were incorporated in the spin-polarized generalized gradient approximation (GGA) using the Perdew–Wang (PW91) functional,<sup>42</sup> and the electron–ion interactions were described by the projector augmented wave (PAW) method.<sup>43,44</sup> A supercell containing 4 Mo atoms and 12 O atoms was used to model the bulk solid, and the number of H atoms in the selected unit cell varies with the concentration of the hydrogen bronze. The Brillouin zone integration was sampled within a  $7 \times 6 \times 2$  Monkhorst–Pack  $k$  point mesh,<sup>45</sup> and electron smearing was employed using the Methfessel–Paxton technique<sup>46</sup> with a width of 0.1 eV to minimize the errors in the Hellmann–Feynman forces. A finer  $k$ -point sampling was used to produce high quality band structure and density of states (DOS). The calculated energies were extrapolated to  $T = 0$  K. Full structural optimizations were performed until the total energy of the system was converged to less than  $10^{-3}$  eV.

We used the nudged elastic band (NEB) method<sup>47</sup> to calculate the minimum energy profile along the prescribed diffusion pathways with the initial and final states chosen based on the optimized absorption structures. The number of images was chosen to achieve smooth curves. To compute atomic charges of the systems, we employed a fast and robust algorithm for Bader decomposition of charge density recently developed by Henkelman and co-workers.<sup>48,49</sup> The Bader charges quoted include both the core charge and the integrated electron density over the atomic basin.

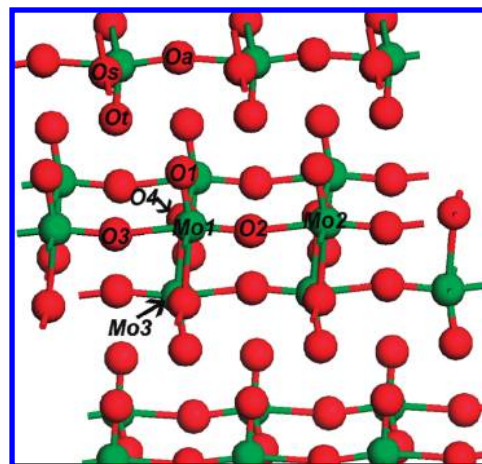


**Figure 1.** Optimized structure of bulk  $\alpha\text{-MoO}_3$ , where the terminal, symmetric bridging, and asymmetric bridging oxygen sites are denoted by  $\text{O}_t$ ,  $\text{O}_s$ , and  $\text{O}_a$ , respectively.

## III. Results and Discussion

Hydrogen spillover takes place by maintaining a pressure of hydrogen in the presence of the catalyst/ $\text{MoO}_3$  system where dissociative chemisorption of  $\text{H}_2$  occurs on the surfaces of the catalyst particles. The H atoms then migrate from the catalyst particle surfaces onto the substrate and subsequently diffuse into the bulk. We have shown in a previous study that H atom migration from the fully hydrogen saturated Pt clusters, which serve as model catalysts, onto the terminal O atoms of the  $\text{MoO}_3$  surface layer is facile.<sup>31</sup> The H atoms are first adsorbed on the terminal O atoms followed by intralayer diffusion. Thus, to understand hydrogen spillover mechanisms in the bulk bronze materials, we need to examine the properties of both H-adsorption and H-diffusion in the lattice since H atom migration from the catalyst to the substrate is a surface phenomenon that was previously investigated.

**3.1. Bulk  $\text{MoO}_3$ .** We first examined the structural and electronic properties of bulk  $\alpha\text{-MoO}_3$ , which has orthorhombic symmetry composed of layers aligned in the (010) orientation. The optimized lattice parameters,  $a = 3.721$  Å,  $b = 3.965$  Å, and  $c = 14.673$  Å, are in reasonable agreement with the experimental data of 3.696, 3.963, and 13.855 Å.<sup>50</sup> The calculated  $c$  parameter is slightly longer than the experimental value due to the fact that the structure of bulk  $\alpha\text{-MoO}_3$  is composed of  $\text{MoO}_3$  slabs along the  $c$ -axis packed together via van der Waals interactions and GGA is known to underestimate such interaction forces. There are three structurally distinctive types of oxygen atoms in bulk  $\text{MoO}_3$ : one-coordinate terminal oxygens,  $\text{O}_t$ ; two-coordinate asymmetric bridging oxygens,  $\text{O}_a$ ; and three-coordinate symmetric bridging oxygens,  $\text{O}_s$ , as shown in Figure 1. The optimized Mo–O bond lengths, shown in Table 1, are in good agreement with available experimental data<sup>50</sup> and previous calculations.<sup>51,52</sup>

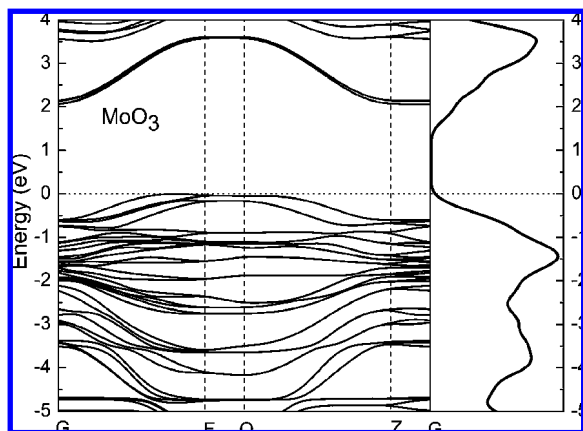
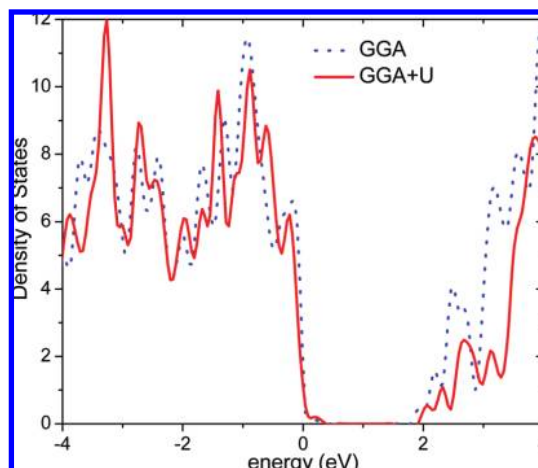
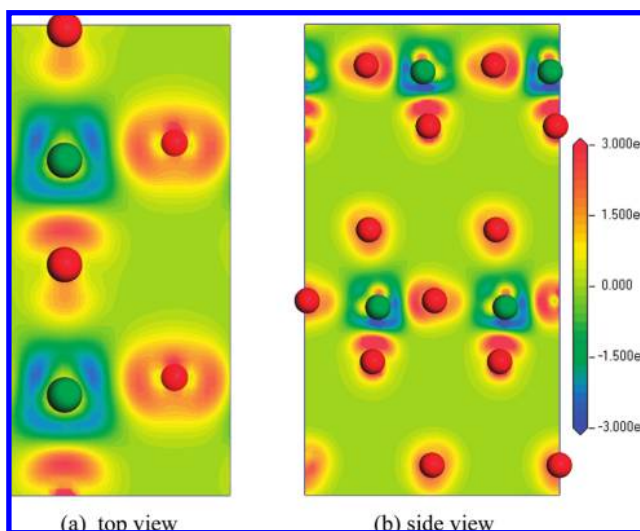
The calculated band structure and electronic density of states (DOS) are displayed in Figure 2, with the Fermi level shifted to zero. The valence band directly below the Fermi level has a width of 5.8 eV, and the gap between the conduction band and the valence band is about 1.9 eV, both in good agreement with previous DFT calculations.<sup>33,52</sup> Experimentally,  $\text{MoO}_3$  was found to be an  $n$ -type semiconductor with a band gap of 3.3 eV.<sup>53</sup> It is not uncommon for DFT calculations to underestimate the band gap of transition metal oxides since the relative energies of occupied and unoccupied electronic levels are not well described.<sup>54</sup> The

**TABLE 1: Bond Parameters and Bader Atomic Charges in the Optimized bulk MoO<sub>3</sub> Structure, in Comparison to Experimental Data**

		calculations	experiment
bond length (Å)	Mo–O <sub>t</sub>	1.702	1.671
	Mo–O <sub>a</sub>	1.774	1.734
		2.211	2.251
	Mo–O <sub>s</sub>	1.962	1.948
		2.429	2.332
Bader charge	Mo	2.29	
	O <sub>t</sub>	–0.56	
	O <sub>s</sub>	–0.95	
	O <sub>a</sub>	–0.77	

DFT+U method was proposed to address the on-site Coulomb interactions more accurately in the localized d or f orbitals in strongly correlated systems by adding an additional Hubbard-type term.<sup>55,56</sup> Wang et al. performed detailed comparisons of the calculated magnetic moments and band gaps for many transition metal oxides using GGA and GGA+U methods, and reported significant improvements with the GGA+U calculations compared with experimental data, especially for ferromagnetic and antiferromagnetic oxides.<sup>57</sup> For diamagnetic transition metal oxides, such as Cu<sub>2</sub>O, V<sub>2</sub>O<sub>5</sub>, and CrO<sub>3</sub>, the change in band gap by adding the Hubbard term was relatively modest. We performed GGA+U calculations for bulk  $\alpha$ -MoO<sub>3</sub> with the U and J parameters at 6.4 and 0.95 eV, respectively.<sup>58</sup> As shown in Figure 3, GGA+U only slightly increased the calculated band gap of bulk  $\alpha$ -MoO<sub>3</sub> by about 0.1 eV, similar to what was found in several other diamagnetic metal oxides.<sup>57</sup> Coquet and Willock reported a band gap of 2.1 eV for bulk  $\alpha$ -MoO<sub>3</sub> based on their DFT+U study, consistent with our results.<sup>33</sup> Since the GGA+U calculations did not show significant improvements to the predicted electronic structure characteristics, we employed only GGA calculations in our H atom absorption and diffusion studies.

The calculated Bader charges of Mo and O atoms in the optimized bulk  $\alpha$ -MoO<sub>3</sub> (Table 1) clearly indicate that the Mo atoms are significantly oxidized by O atoms with the symmetric bridging oxygen bearing the largest negative charge due to its high coordination number. The terminal oxygen, however, is more strongly electron withdrawing because of its unsaturated valence, and both the symmetric and asymmetric bridging oxygen atoms exhibit considerable ionic character. The calculated charges agree with the previous Bader population analysis by Coquet and Willock,<sup>33</sup>

**Figure 2.** Band structure and electronic density of state of bulk  $\alpha$ -MoO<sub>3</sub>. All of the energies are relative to the Fermi level.**Figure 3.** Electronic density of state of bulk  $\alpha$ -MoO<sub>3</sub> calculated from GGA+U method, in comparison to the GGA results.**Figure 4.** Calculated electronic density distributions in optimized  $\alpha$ -MoO<sub>3</sub> structure. The locations of Mo and O atoms are denoted by green and red spheres.

and the slight differences likely arise from the fact that, while we used fully optimized structures, the lattice parameter along the *c* direction was fixed at the experimental value in Coquet and Willock's calculations. Electron population analysis based on the Milliken scheme also led to similar conclusions.<sup>35</sup> The calculated electronic density differences between bulk  $\alpha$ -MoO<sub>3</sub> with respect to the atomic densities clearly shows that all O atoms are withdrawing electrons from their neighboring Mo atoms, as shown in Figure 4. The charges around the asymmetric oxygen are unequally distributed toward two neighboring Mo atoms due to the different Mo–O bond lengths, and the charges around the symmetric oxygen atoms are evenly distributed toward two neighboring Mo atoms in the plane. Most of the electron density around the terminal oxygen lies along the Mo–O bond, indicating a considerably covalent character for this bond.

**3.2. H Atom Absorption.** To understand the relative reactivity of MoO<sub>3</sub> toward hydrogen spillover and the hydrogen desorption dynamics from the bronzes, we next examined the structural, energetic and electronic properties for H atoms residing in the MoO<sub>3</sub> lattice at various H atom concentrations. The fully optimized absorption configurations are shown in Figure 5. The calculated lattice parameters and the average



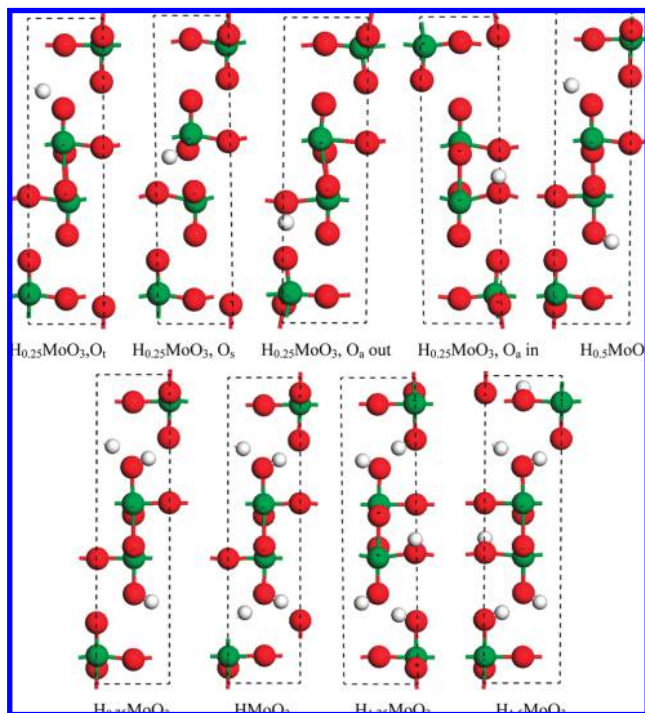


**Figure 5.** Fully optimized configurations for hydrogen molybdenum bronze,  $H_x\text{MoO}_3$ , at different H atom concentrations and binding sites and modes. Mo, O, and H atoms are represented by green, red, and white spheres, respectively.

**TABLE 2: Lattice Parameters and H Absorption Energies of  $H_x\text{MoO}_3$  at Various H Atom Concentrations, in Comparison to Available Experimental Data**

		$a$ (Å)	$b$ (Å)	$c$ (Å)	$\beta$ (°)	$E_{\text{absorp}}$ (eV)
$\alpha\text{-MoO}_3$	calculations	3.721	3.965	14.673	90	
	experiment	3.696	3.963	13.855	90	
$H_{0.25}\text{MoO}_3$	$O_t$	3.769	3.824	15.544	90	2.90
	$O_s$	3.799	3.800	15.615	90	2.32
	$O_a$ , up	3.734	4.055	14.853	90	2.45
	$O_a$ , down	3.760	3.914	15.429	90	2.87
	experiment <sup>a</sup>	3.718	3.890	14.18	90	
$H_{0.5}\text{MoO}_3$	$H_{0.28}\text{MoO}_3$					
	calculations	3.772	3.821	15.769	90.5	2.85
	experiment <sup>a</sup>	3.769	3.852	14.543	90.7	
$H_{0.75}\text{MoO}_3$	$H_{0.6}\text{MoO}_3$					
	calculations	3.759	3.827	16.113	90.4	2.79
$\text{HMoO}_3$	calculations	3.727	3.834	16.196	90.3	2.73
	experiment <sup>a</sup>	3.794	3.862	14.519	93.7	
	$H_{0.9}\text{MoO}_3$					
$H_{1.25}\text{MoO}_3$	calculations	3.765	3.892	16.264	90.6	2.57
	calculations	3.784	3.983	16.058	91.0	2.42
$H_{1.5}\text{MoO}_3$	experiment <sup>b</sup>	3.774	4.059	19.927	93.94	
	$H_{1.67}\text{MoO}_3$					

<sup>a</sup> Reference 59. <sup>b</sup> Reference 60.

absorption energies of H atoms at various concentrations are listed in Table 2. Here, the average absorption energies are defined as

$$E_{\text{absorp}} = \frac{1}{x} [E(\text{MoO}_3) + xE(\text{H}) - E(\text{H}_x\text{MoO}_3)]$$

where  $E(\text{H}_x\text{MoO}_3)$ ,  $E(\text{H})$ , and  $E(\text{MoO}_3)$  are the total energies of the  $\text{H}_x\text{MoO}_3$  bronze, gas phase atomic hydrogen, and bulk  $\alpha\text{-MoO}_3$ , respectively. At higher H atom concentrations, the lattice parameters of  $a$  and  $b$  change only modestly while the  $c$  parameter increases more rapidly. For  $\text{H}_{0.25}\text{MoO}_3$ , the bronze has the same orthorhombic crystal structure as bulk  $\alpha\text{-MoO}_3$ ,

with the lattice angles  $\alpha$ ,  $\beta$ , and  $\gamma$  all at  $90^\circ$ . Further increases in the hydrogen concentration leads to a slight deviation of  $\beta$  from  $90^\circ$  while  $\alpha$  and  $\gamma$  stay at  $90^\circ$ , making the bronze structure monoclinic. Experimentally, the molybdenum bronze was found to have a maximum  $x$  value of 2.0. Four different hydrogen molybdenum bronze phases were identified depending on the H atom concentration. Phases I ( $0.25 < x < 0.40$ ) and II ( $0.85 < x < 1.04$ ) are both blue in color with orthorhombic and monoclinic crystal structures, respectively. Phases III ( $1.55 < x < 1.72$ ) and IV ( $x = 2.0$ ) are monoclinic with red and green colors, respectively.<sup>30</sup> Compared to the experimentally available lattice parameters with similar H atom concentrations,<sup>59,60</sup> our GGA calculations consistently overestimate the  $c$  values due to the intrinsic inaccuracy of the method in describing weak van der Waals interactions between the layers, but the calculated bonding structures within the  $\text{MoO}_3$  layers are in good agreement with the experimental results.

At a low H atom concentration of  $\text{H}_{0.25}\text{MoO}_3$ , we calculated the absorption energies and configurations for H atoms on all three types of oxygen atoms in the lattice.

1. On the symmetric bridging oxygen, the hydrogen is bound in the (010) plane with an absorption energy of 2.45 eV. H atom absorption lengthens the Mo–O bonds between the symmetric bridging oxygen and its neighboring Mo atoms, increasing the Mo–O bond length from 1.96 to 2.05 Å in the plane and from 2.43 to 2.68 Å between the symmetric O with Mo atom in the adjacent plane.

2. On the asymmetric bridging oxygen, the hydrogen is bound in two different modes: perpendicular to the (010) plane or at an angle pointing directly toward the inside of the layer, with H binding energies of 2.32 and 2.87 eV, respectively. Substantial lattice relaxation occurs upon H atom absorption in both cases with the two unequal Mo–O bond lengths of 1.77 Å and 2.21 Å in bulk  $\alpha\text{-MoO}_3$  becoming essentially equal in length at 2.03 Å.

3. On the terminal oxygen, the H atom is bound with an angle of  $60^\circ$  normal to the (010) plane with a relatively high binding energy of 2.90 eV due to the unsaturated valence of the O atom. The Mo–O bond length between the terminal oxygen and its neighboring Mo is significantly elongated from 1.70 Å to 1.88 Å.

The H atom coordination in the bulk exhibits significant differences from what was observed on the (010) surface. First, the terminal oxygen is the most favorable H atom absorption site in the bulk but only a metastable, weak binding site on the surface due to different lattice bonding environments.<sup>31</sup> In the bulk, H atoms not only bind directly with oxygen via a strong O–H bond (ca. 0.98 Å) but also interact with the two terminal oxygen atoms in the adjacent layers via a weaker hydrogen bond (2.33 Å). The latter bonding mode is absent on the (010) surface. Despite the experimental studies to date, the exact locations of the H atoms in the bronze materials remain an open topic of research. Ritter et al. suggest that H atoms first fill the intralayer positions on the asymmetric bridging oxygen atoms at an angle oriented toward the inside of the layer, and then start to fill the terminal oxygen sites when the H atom concentration is in excess  $x = 0.85$ .<sup>26</sup> However, a recent combined theoretical and experimental study suggests no hydrogen occupation on the intralayer sites, even at high H atom concentrations in phase III.<sup>60</sup> Adams examined the location of absorbed H atoms using a combination of time-resolved X-ray diffraction with molecular mechanics simulations and derived a structural model for phase II hydrogen bronze with H atoms absorbed on terminal oxygens.<sup>59</sup> Our results indicate that the calculated H binding

**TABLE 3: Bond Length Changes Introduced by the Absorption of H at Low Concentration in  $\text{H}_{0.25}\text{MoO}_3$ <sup>a</sup>**

H absorption site		bond length ( $\text{\AA}$ )	
		$\alpha$ - $\text{MoO}_3$	$\text{H}_{0.25}\text{MoO}_3$
terminal oxygen O1	Mo1–O1	1.702	1.876
	Mo1–O2	1.774	1.895
	Mo1–O3	2.211	1.929
	Mo1–O4	1.962	1.932
symmetric oxygen O4	Mo3–O4	2.429	2.681
	Mo1–O4	1.962	2.054
	Mo1–O3	2.211	1.921
	Mo1–O2	1.774	1.948
asymmetric oxygen O2, up	Mo1–O2	1.774	2.028
	Mo2–O2	2.211	2.047
	Mo1–O1	1.702	1.712
	Mo1–O3	1.962	1.950
asymmetric oxygen O2, down	Mo1–O2	1.774	2.024
	Mo2–O2	2.211	2.023
	Mo2–O1	1.702	1.685
	Mo1–O3	1.962	1.946

<sup>a</sup> Different Mo and O sites, from Mo1 to Mo3, and O1 to O4, are denoted in Figure 1.

energies on the terminal and asymmetric oxygen atoms differ only by 0.03 eV, suggesting that these two sites can both be populated upon hydrogen spillover. In practice, the distribution of the absorbed H atoms would likely depend on the preparation of the samples, which is probably one of the reasons why the locations of H atoms in the bronze materials found in different experiments differ from each other.<sup>26,59,60</sup> The calculated average H atom absorption energies shown in Table 2 indicate that as the H atom content in the lattice increases, the H atom binding strength decreases, assuming that at a given H atom concentration the H atoms always fill the lowest energy absorption sites first.

We found that the O–H bond lengths (0.99  $\text{\AA}$ ) in the optimized  $\text{H}_{0.25}\text{MoO}_3$  structure are essentially independent of the absorption site. However, the absorption significantly changes the nature of the Mo–O bonding near the absorption sites. As shown in Table 3, the Mo–O bond length between the oxygen where H is absorbed and the neighboring Mo atoms is generally elongated. In  $\alpha$ - $\text{MoO}_3$ , Mo forms bonds with two neighboring asymmetric oxygen atoms with distinctively different bond lengths of 1.774 and 2.211  $\text{\AA}$ , respectively. Upon H absorption, the two unequal Mo–O bond lengths become essentially equal with 1.91, 1.93, and 2.03  $\text{\AA}$  for H absorption on the terminal, symmetric and asymmetric oxygen sites, respectively.

To model higher H atom concentrations in the molybdenum bronze materials, we adopted a procedure to place H atoms in the lattice based on the energetic preference of absorption sites. Specifically, the most favorable terminal oxygen sites are populated first, followed by the asymmetric oxygen sites. Table 4 shows the distribution of H atoms in the selected hydrogen bronze materials. The average adsorption energy decreases significantly with the increase of H atom loading, as shown in Table 2, while the optimized O–H bond distances are relatively unaffected.

The calculated band structures and densities of states for several selected hydrogen bronzes are shown in Figure 6. In contrast to the semiconductor-like band structure of bulk  $\alpha$ - $\text{MoO}_3$ , the band structures of all of the hydrogen bronzes exhibit strong metallic features with considerably widened valence bands across the Fermi level into the conduction bands. The abrupt change of electronic structures of the hydrogen

**TABLE 4: Distribution of H Atoms on Different Oxygen Sites in the Unit Cell of Hydrogen Molybdenum Bronze with 4 Mo and 12 O Atoms at Various Concentrations of  $\text{H}_x\text{MoO}_3$ <sup>a</sup>**

	O <sub>t</sub>	O <sub>a</sub>	O <sub>s</sub>
$\text{H}_{0.25}\text{MoO}_3$	1	0	0
$\text{H}_{0.5}\text{MoO}_3$	2	0	0
$\text{H}_{0.75}\text{MoO}_3$	3	0	0
$\text{HMoO}_3$	4	0	0
$\text{H}_{1.25}\text{MoO}_3$	4	2	0
$\text{H}_{1.5}\text{MoO}_3$	4	2	0

<sup>a</sup> The terminal, symmetric bridging, and asymmetric bridging oxygen sites are denoted by O<sub>t</sub>, O<sub>s</sub>, and O<sub>a</sub>, respectively.

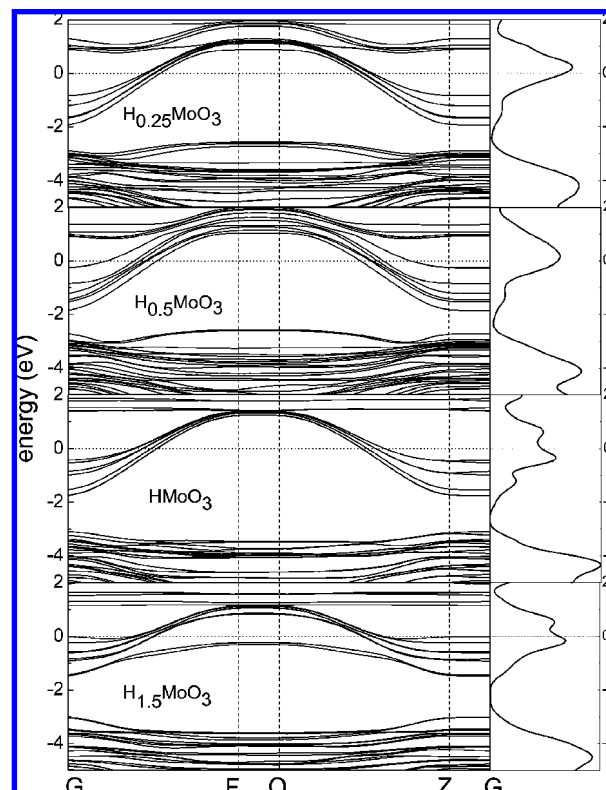


**Figure 6.** Band structures and electronic densities of state for several hydrogen molybdenum bronzes,  $\text{H}_{0.25}\text{MoO}_3$ ,  $\text{H}_{0.5}\text{MoO}_3$ ,  $\text{HMoO}_3$ , and  $\text{H}_{1.5}\text{MoO}_3$ . The energies are relative to the Fermi level.

**TABLE 5: Bader Atomic Charges in Hydrogen Molybdenum Bronze,  $\text{H}_x\text{MoO}_3$ , in Comparison to Bulk  $\text{MoO}_3$** 

	$\text{H}_{0.25}\text{MoO}_3$	$\text{H}_{0.5}\text{MoO}_3$	$\text{H}_{0.75}\text{MoO}_3$	$\text{HMoO}_3$	$\text{MoO}_3$
H	0.67	0.67	0.66	0.69	
bond O <sub>t</sub>	−0.97	−0.96	−1.07	−0.96	−0.56
neighboring Mo	2.25	2.19	2.20	2.18	2.29

bronzes arises from the strong H-bonding network formed upon H absorption and the subsequent charge transfer. The highly polarized bonding environment in the lattice gives rise to higher electron mobility, which makes the bronzes strongly metallic. This agrees well with the experimental findings, which shows that semiconducting molybdenum oxide becomes a metallic conducting hydrogen bronze upon H atom absorption.<sup>29</sup>

We next performed Bader charge analysis on the hydrogen bronzes with various H atom concentrations, as shown in Table 5. Upon H atom absorption onto the terminal oxygen, charge transfer occurs from the H 1s orbital to the O 2p orbital and the H atom becomes essentially protonic. The terminal O atom

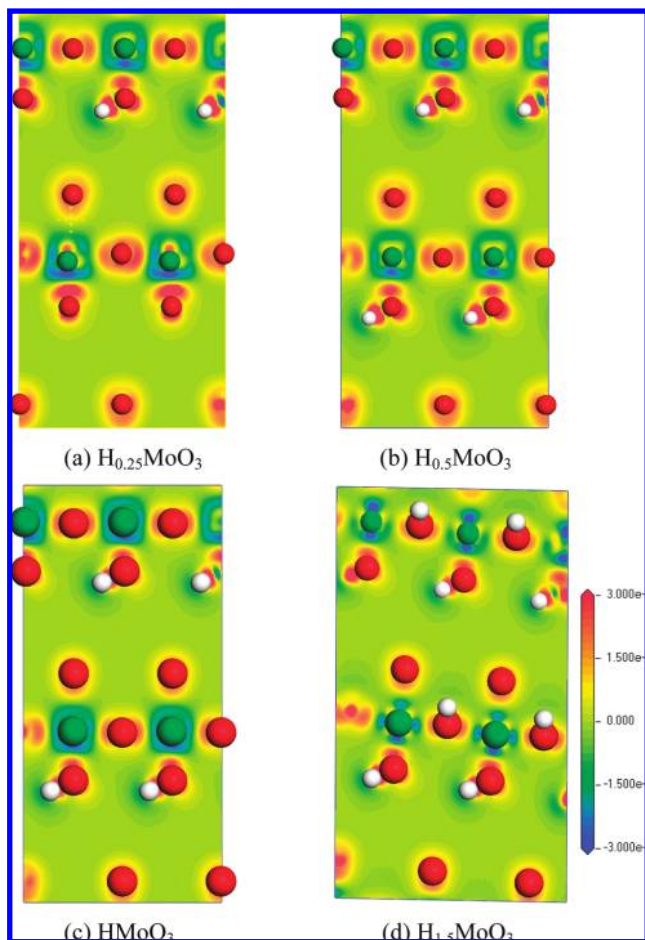


**Figure 7.** Electronic density distributions in an optimized  $\text{H}_{0.25}\text{MoO}_3$  structure, with the H atom absorbed on a terminal oxygen site. The locations of the Mo, O, and H atoms are denoted by green, red, and white spheres, respectively.

then transfers the extra charge to the Mo atoms in direct coordination. Consequently, the Mo atoms are moderately reduced and the Mo–O bond strength is slightly decreased. The Bader charge analysis is consistent with the calculated electron density maps shown in Figure 7. At all four selected H atom concentrations, there is clearly charge transfer from the absorbed H atom toward the neighboring terminal oxygen. The charge on the terminal oxygen is readjusted accordingly and the charges around its neighboring Mo atoms are much more evenly distributed due to the charge transfer and lattice reconstruction induced by the absorption of the H atoms. The charge transfer and lattice reconstruction are not localized to only the immediate vicinity of the absorption site. For H atom absorption on terminal oxygen atoms, the electron density around the nearby asymmetric bridging O atoms is evenly distributed toward their neighboring Mo atoms, significantly different than the uneven electron density distribution in bulk  $\alpha\text{-MoO}_3$  due to the highly inequivalent Mo–O bond lengths (Figure 4). A previous atomic force microscopy and X-ray diffraction study by Smith and Rohrer demonstrated that  $\text{MoO}_3$  intercalates H and the protonation of H leads to the precipitation of hydrogen bronze.<sup>25</sup> Eda et al. examined the locations of protons in  $\text{H}_{0.26}\text{MoO}_3$  by line shape analysis and suggested that 3- to 5-proton clusters may exist in the bronze.<sup>61</sup> The formation of protonic hydrogen and the enhancement of hydrogen spillover has also been studied by NMR spectroscopy in other transition metal oxides such as  $\text{CeO}_2$ .<sup>7</sup> Our results are consistent with these experimental observations.

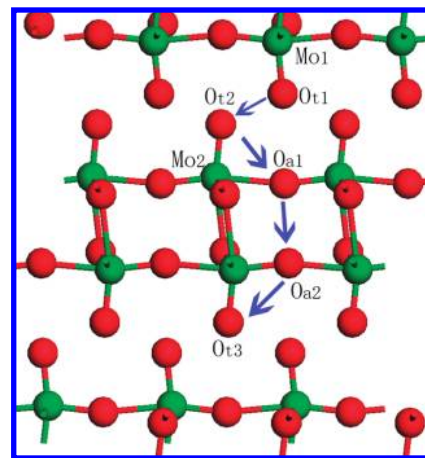


**Figure 8.** Schematic plot of H atom diffusion pathway in bulk  $\text{MoO}_3$ .

**3.3. H Atom Diffusion.** To gain insight into hydrogen spillover and the mechanism of H atom migration within a crystalline metal oxide lattice, we performed nudged elastic band calculations to examine the minimum energy pathways for an H atom to diffuse in the lattice of molybdenum hydrogen bronze. Due to the computational intensity of these calculations, we performed this analysis only for  $\text{H}_{0.25}\text{MoO}_3$ . At this low H atom concentration, the terminal oxygen atoms and asymmetric oxygen atoms with an angle pointing inside the layer are the two most favorable H atom absorption sites with calculated H binding energies of 2.90 and 2.87 eV, respectively. These two sites are most likely involved in the H atom diffusion processes since H atom binding on other adsorption sites is much less energetically favorable. The diffusion pathway selected in our minimum energy path calculations is shown schematically in Figure 8. The H atom, initially adsorbed on a terminal oxygen ( $\text{O}_{t1}$ ), first transfers to another terminal oxygen site ( $\text{O}_{t2}$ ) in the adjacent layer; it continues migrating inside the layer to an adjacent asymmetric site ( $\text{O}_{a1}$ ), then moves again to the next neighboring asymmetric site ( $\text{O}_{a2}$ ), ceasing diffusion at another terminal oxygen site ( $\text{O}_{t3}$ ). The migration of hydrogen between  $\text{O}_{a2}$  and  $\text{O}_{t3}$  is the reverse process from  $\text{O}_{t2}$  to  $\text{O}_{a1}$  with essentially the same diffusion barrier. We first performed NEB calculations to estimate the activation energy barrier for a chemisorbed H on the terminal oxygen to rotate around the axis parallel to the (010) layer. The calculated activation energy was found to be essentially zero. Similarly, the calculated activation barrier for the H atom on the asymmetric oxygen to rotate along the direction pointing to the inner layer is also negligible. We subsequently carried out minimum energy path calculations along the H atom diffusion route defined by  $\text{O}_{t1} \rightarrow \text{O}_{t2} \rightarrow \text{O}_{a1} \rightarrow \text{O}_{a2}$  in Figure 8. The calculated energy profile is displayed in Figure 9. The H atom migrates readily from one terminal oxygen to the nearest terminal oxygen of the adjacent layer with a low energy barrier of 0.13 eV. The barrier for a H atom to move from  $\text{O}_{t2}$  to  $\text{O}_{a1}$  is estimated to be only 0.10 eV and the barrier for migration from  $\text{O}_{a1}$  to  $\text{O}_{a2}$  is even smaller (0.06 eV). Ritter et al. have performed solid state  $^1\text{H}$  NMR studies to examine the bonding properties, location, and H atom mobility in  $\text{H}_x\text{MoO}_3$ , and reported an activation energy for H diffusion on the order of 0.1–0.3 eV.<sup>26</sup> Our calculated activation barriers are in good agreement with this experimental value range. The small migration barriers for protons in the lattice indicate that H atom diffusion in the  $\text{MoO}_3$  lattice is feasible. Therefore, this is the ultimate reason why hydrogen spillover occurs with such facility in this class of materials.



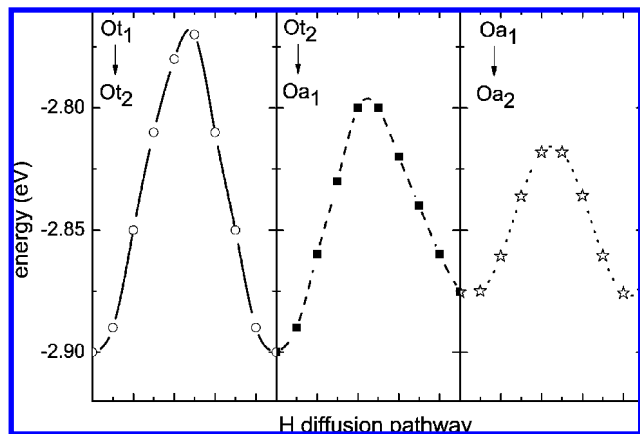


**Figure 9.** Calculated energy profile for H atoms to migrate within the hydrogen molybdenum bronze,  $H_{0.25}MoO_3$ , from one terminal oxygen to its neighboring terminal oxygen in an adjacent layer, and further to two adjacent asymmetric oxygen absorption sites.

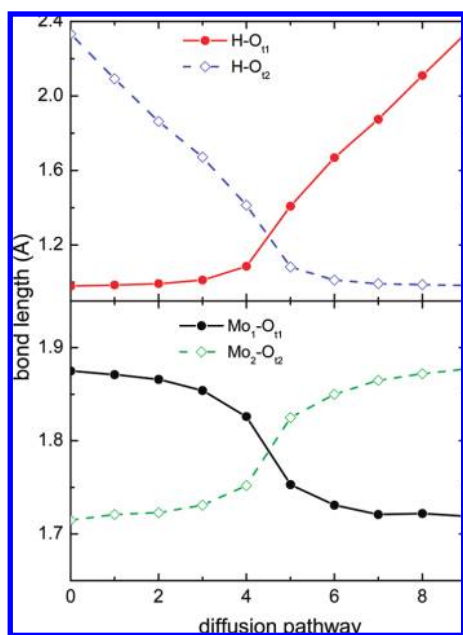


**Figure 10.** Evolution of H–O and Mo–O bond distances for H migration from one terminal oxygen,  $O_{t1}$ , to its neighboring oxygen,  $O_{t2}$ , in the adjacent layer.  $Mo_1$  and  $Mo_2$  are the two neighboring Mo atoms to the terminal oxygen atoms  $O_{t1}$  and  $O_{t2}$ , respectively.

To explore the geometric and electronic structural evolution during the H atom diffusion process, we monitored the variation of the main bond parameters and Bader charges as a H atom diffuses from one terminal oxygen atom,  $O_{t1}$ , to its neighboring terminal oxygen in the adjacent layer,  $O_{t2}$ . This is likely the rate determining step of the spillover process. The change of primary bonding parameters during this diffusion step is shown in Figure 10. The H– $O_{t1}$  distance remains essentially steady until the transition state is reached, at which point the H– $O_{t1}$  bond is partially broken to form a new H– $O_{t2}$  bond. The evolution of the H– $O_{t2}$  distance is essentially the reverse of the H– $O_{t1}$  distance. The H atom transfer thus adopts a “jumping” mode, which explains why the barrier is the highest along our prescribed diffusion pathway. As hydrogen migrates from  $O_{t1}$  to  $O_{t2}$ , the  $Mo_1$ – $O_{t1}$  bond is shortened from 1.87 to 1.72 Å, while the  $Mo_2$ – $O_{t2}$  bond becomes elongated, representing a stronger  $Mo_1$ – $O_{t1}$  bond and a weaker  $Mo_2$ – $O_{t2}$  bond, respectively. The variation of the Mo–O bonds reflects the change of the oxidation states of the Mo atoms upon H

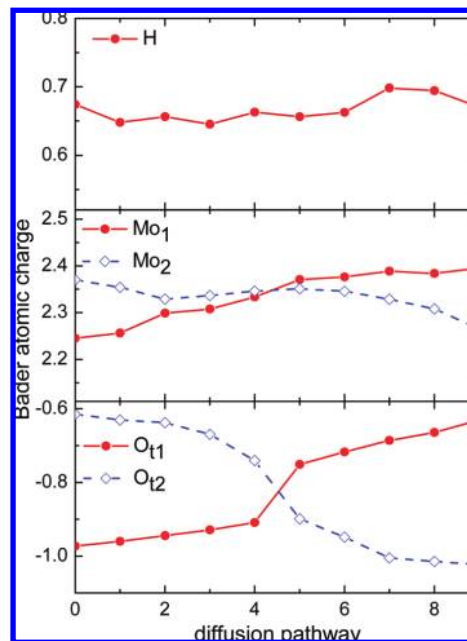


**Figure 11.** Change in the Bader atomic charge for H, Mo, and O atoms for H migration from one terminal oxygen,  $O_{t1}$ , to its neighboring oxygen,  $O_{t2}$ , in the adjacent layer.  $Mo_1$  and  $Mo_2$  are the two neighboring Mo atoms to the terminal oxygen atoms  $O_{t1}$  and  $O_{t2}$ , respectively.

migration. Figure 11 displays the calculated Bader charges along the H atom diffusion pathway. The charge on the mobile hydrogen fluctuates only slightly in a range between 0.65 and 0.7 e, indicating that the hydrogen remains essentially protonic. The terminal oxygen gains an extra 0.4 e upon H absorption, and the charge is reduced to  $\sim -0.6$  e after the H release. Consequently, the Mo atom adjacent to the site where H is absorbed gains approximately 0.14 e, indicating that the metal atom is partially reduced and thus the Mo–O bond becomes slightly weaker. In contrast, the Mo atom without H absorption on the adjacent O atoms is more positively charged, suggesting a higher oxidation state and hence a stronger Mo–O bond. At the transition state, the  $Mo_1$  and  $Mo_2$  atoms share essentially the same Bader charge and so do the  $O_{t1}$  and  $O_{t2}$  atoms, consistent with the equal Mo–O and H–O bond lengths at the transition state.

**3.4. H Atom Desorption.** For hydrogen storage purposes, molybdenum and tungsten hydrogen bronzes are not practical since the gravimetric storage capacity is relatively low because the presence of “heavy” elements with high atomic weights. However, because of the ability to reversibly capture hydrogen,  $MoO_3$  has been used as a hydrogen reservoir in hydrogenation catalysis,<sup>19,20</sup> and for the study of other spillover-based hydrogen storage materials, it is important to understand the desorption of hydrogen from metal oxides. As a measure of hydrogen desorption capability, we calculated the sequential desorption energy to form  $H_2$  molecules from several selected hydrogen bronzes with varying H atom concentrations, defined by

$$\Delta E_{\text{des}}^x = 8 \left[ E(H_{x-0.25}MoO_3) + \frac{1}{8} E(H_2) - E(H_x MoO_3) \right] \quad (1)$$

Here, we assume that at a given H atom concentration the H atoms always occupy the most stable absorption sites first. This assumption is justified in light of the fact that H atom diffusion in the lattice is facile and thus thermal equilibration can be



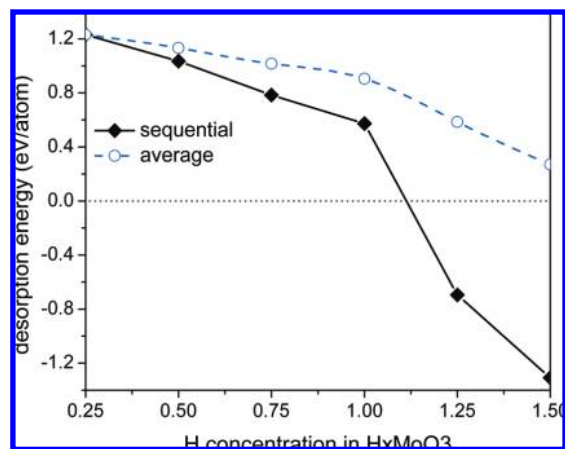


**Figure 12.** Calculated sequential desorption energies for hydrogen molybdenum bronze at different H atom concentrations.

reached quickly. The sequential desorption energy measures the energy required to remove a  $H_2$  molecule from the bronze at a given H loading; the reference state is selected as the ground-state of the bronze after the  $H_2$  removal. The calculated results are displayed in Figure 12, where, for comparison purpose, we also show the calculated average adsorption energies defined by

$$\Delta E_{\text{des}}^A = 2 \left[ E(\text{MoO}_3) + \frac{x}{2} E(\text{H}_2) - E(\text{H}_x\text{MoO}_3) \right] / x \quad (2)$$

As expected, the sequential desorption energy decreases as H loading increases, and desorption becomes an exothermic process at H loading higher than  $x = 1$ , indicating that it becomes increasingly difficult for the lattice to accommodate the H atoms and the materials are in a thermally unstable condition. The results thus suggest that desorption is facile at medium to high H loading. The calculated average desorption energy decreases monotonically. However, it remains endothermic in the entire range of the selected H loadings.

#### IV. Summary

Hydrogen spillover in carbon based materials has emerged as one of the most important techniques to store hydrogen. Understanding of the spillover mechanism is essential for design and development of novel materials for hydrogen storage under near-ambient conditions. To this end, it is beneficial to understand the spillover mechanism in transition metal oxides that has observed experimentally and studied in great detail. The main purpose of the present study is to explore the atomistic details of spillover process in bulk  $\alpha\text{-MoO}_3$ .

We performed detailed DFT calculations to study the two main components of hydrogen spillover in  $\alpha\text{-MoO}_3$ , the absorption and diffusion of atomic hydrogen. We first calculated structure of bulk  $\alpha\text{-MoO}_3$ . The optimized lattice parameters are in good agreement with the experimental values and the calculated electronic structure of this material exhibits a typical semiconductor band gap. Upon incorporation of H atoms at various concentrations into  $\alpha\text{-MoO}_3$ , hydrogen molybdenum bronze materials,  $H_x\text{MoO}_3$ , are formed and the crystalline lattices undergo significant relaxation near the absorption sites. Energetically most favorable binding sites were identified. In particular, our results indicate that the two most preferred absorption sites, the terminal and asymmetric oxygen atoms, interact with H atoms with nearly equal bond strength.

Consequently, they may both be populated upon H atom absorption, which is likely the reason why the precise locations of H atoms in the lattice vary in different experiments, depending on sample preparation.

Hydrogen absorption in  $\alpha\text{-MoO}_3$  results in an extensive hydrogen bonding network in the crystalline lattice. As a consequence, the hydrogen molybdenum bronze materials were all found to be metallic with the valence band widened across the Fermi level and into the conduction band, consistent with experimental observations. The Bader population analysis indicates that absorbed H atoms lose electron density, becoming protonic in nature. The charge transfer from hydrogen to the O atom, on which the H atom resides, gives rise to the reduction on the adjacent Mo atom and thus a weaker Mo–O bond.

To understand the mobility of the H atoms in the lattice, we performed calculations on H atom diffusion in bulk  $\alpha\text{-MoO}_3$  along a prescribed diffusion pathway. Our results indicate that the protonic hydrogen diffuses with very small activation barriers, suggesting that these H atoms should be highly mobile at near-ambient temperatures. The calculated barrier heights lie well within the range of experimentally measured values. The high mobility of H atoms in the lattice, facilitated by the massive hydrogen bonding network, reflects the essence of the spillover mechanism in these materials. Our study shows that hydrogen desorption to form  $H_2$  molecules is an exothermic process for hydrogen bronzes with a H concentration higher than  $H\text{MoO}_3$  and becomes endothermic at low H loadings.

**Acknowledgment.** The authors gratefully acknowledge partial funding for this work provided by the U.S. Department of Energy's Office of Energy Efficiency and Renewable Energy via the Hydrogen Sorption Center of Excellence (contract DE-FC-05GO15074).

#### References and Notes

- (1) Cheng, H.; Chen, L.; Cooper, A. C.; Sha, X. W.; Pez, G. P. *Energy Environ. Sci.* **2008**, *1*, 338.
- (2) Conner, W. C.; Falconer, J. L. *Chem. Rev.* **1995**, *95*, 759.
- (3) Lachawiec, A. J.; Qi, G. S.; Yang, R. T. *Langmuir* **2005**, *21*, 11418.
- (4) Li, Y. W.; Yang, R. T. *J. Am. Chem. Soc.* **2006**, *128*, 8136.
- (5) Li, Y. W.; Yang, R. T. *J. Am. Chem. Soc.* **2006**, *128*, 726.
- (6) Li, Y. W.; Yang, R. T. *AIChE J.* **2008**, *54*, 269.
- (7) Dutta, G.; Waghmare, U. V.; Baidya, T.; Hegde, M. S. *Chem. Mater.* **2007**, *19*, 6430.
- (8) Zacharia, R.; Rather, S. U.; Hwang, S. W.; Nahm, K. S. *Chem. Phys. Lett.* **2007**, *434*, 286.
- (9) Liu, Y. Y.; Ju-Lan, Z.; Jian, Z.; Xu, F.; Sun, L. X. *Int. J. Hydrog. Energy* **2007**, *32*, 4005.
- (10) Chen, C. H.; Huang, C. C. *Int. J. Hydrog. Energy* **2007**, *32*, 237.
- (11) Chen, C. H.; Huang, C. C. *Microporous Mesoporous Mater.* **2008**, *109*, 549.
- (12) Zielinski, M.; Wojcieszak, R.; Monteverdi, S.; Mercy, M.; Bettahar, M. M. *Int. J. Hydrog. Energy* **2007**, *32*, 1024.
- (13) Li, Y.; Yang, R. T.; Liu, C. J.; Wang, Z. *Ind. Eng. Chem. Res.* **2007**, *46*, 8277.
- (14) Mitchell, P. C. H.; Ramirez-Cuesta, A. J.; Parker, S. F.; Tomkinson, J.; Thompson, D. J. *Phys. Chem. B* **2003**, *107*, 6838.
- (15) Chen, L.; Cooper, A. C.; Pez, G. P.; Cheng, H. *J. Phys. Chem. C* **2007**, *111*, 18995.
- (16) Chen, L.; Pez, G.; Cooper, A. C.; Cheng, H. *J. Phys.-Condensed Matter* **2008**, *20*, 064223.
- (17) Sha, X. W.; Knippenberg, M. T.; Cooper, A. C.; Pez, G. P.; Cheng, H. S. *J. Phys. Chem. C* **2008**, *112*, 17465.
- (18) Li, Y. W.; Yang, F. H.; Yang, R. T. *J. Phys. Chem. C* **2007**, *111*, 3405.
- (19) Hoangvan, C.; Zegaoui, O. *Appl. Catal. A* **1995**, *130*, 89.
- (20) Hoang-Van, C.; Zegaoui, O. *Appl. Catal. A* **1997**, *164*, 91.
- (21) Noh, H.; Wang, D.; Luo, S.; Flanagan, T. B.; Balasubramaniam, R.; Sakamoto, Y. *J. Phys. Chem. B* **2004**, *108*, 310.
- (22) Rodriguez, N. M.; Baker, R. T. K. *J. Catal.* **1993**, *140*, 287.
- (23) Breyse, M.; Furimsky, E.; Kasztelan, S.; Lacroix, M.; Perot, G. *Catal. Rev.-Sci. Eng.* **2002**, *44*, 651.
- (24) Smith, R. L.; Rohrer, G. S. *J. Catal.* **1996**, *163*, 12.

- (25) Smith, R. L.; Rohrer, G. S. *J. Catal.* **1998**, *173*, 219.
- (26) Ritter, C.; Muller-Warmuth, W.; Schollhorn, R. *J. Chem. Phys.* **1985**, *83*, 6130.
- (27) Ritter, C.; Muller-Warmuth, W.; Spiess, H. W.; Schollhorn, R. *Ber. Bunsen-Ges. Phys. Chem.* **1982**, *86*, 1101.
- (28) Dickens, P. G.; Birtill, J. J.; Wright, C. J. *J. Solid State Chem.* **1979**, *28*, 185.
- (29) Whittingham, M. S. *Solid State Ionics* **2004**, *168*, 255.
- (30) Rousseau, R.; Canadell, E.; Alemany, P.; Galvan, D. H.; Hoffmann, R. *Inorg. Chem.* **1997**, *36*, 4627.
- (31) Chen, L.; Cooper, A. C.; Pez, G. P.; Cheng, H. J. *Phys. Chem. C* **2008**, *112*, 1755.
- (32) Chen, L.; Cooper, A. C.; Pez, G. P.; Cheng, H. S. *J. Phys. Chem. C* **2007**, *111*, 5514.
- (33) Coquet, R.; Willock, D. J. *Phys. Chem. Chem. Phys.* **2005**, *7*, 3819.
- (34) Sayede, A.; Khelifa, B.; Mathieu, C.; Aourag, H. *J. Theor. Comput. Chem.* **2003**, *2*, 245.
- (35) Yin, X. L.; Han, H. M.; Miyamoto, A. *J. Mol. Model.* **2001**, *7*, 207.
- (36) Chen, M.; Friend, C. M.; Kaxiras, E. *J. Am. Chem. Soc.* **2001**, *123*, 2224.
- (37) Yuan, S. P.; Wang, J. G.; Li, Y. W.; Peng, S. Y. *Catal. Today* **2000**, *61*, 243.
- (38) Chen, M.; Friend, C. M.; Kaxiras, E. *J. Chem. Phys.* **2000**, *112*, 9617.
- (39) Chen, M.; Waghmare, U. V.; Friend, C. M.; Kaxiras, E. *J. Chem. Phys.* **1998**, *109*, 6854.
- (40) Kresse, G.; Furthmuller, J. *Comput. Mater. Sci.* **1996**, *6*, 15.
- (41) Kresse, G.; Furthmuller, J. *Phys. Rev. B* **1996**, *54*, 11169.
- (42) Perdew, J. P.; Chevary, J. A.; Vosko, S. H.; Jackson, K. A.; Pederson, M. R.; Singh, D. J.; Fiolhais, C. *Phys. Rev. B* **1992**, *46*, 6671.
- (43) Blochl, P. E. *Phys. Rev. B* **1994**, *50*, 17953.
- (44) Kresse, G.; Joubert, D. *Phys. Rev. B* **1999**, *59*, 1758.
- (45) Monkhorst, H. J.; Pack, J. D. *Phys. Rev. B* **1976**, *13*, 5188.
- (46) Methfessel, M.; Paxton, A. T. *Phys. Rev. B* **1989**, *40*, 3616.
- (47) Mills, G.; Jonsson, H.; Schenter, G. K. *Surf. Sci.* **1995**, *324*, 305.
- (48) Henkelman, G.; Arnaldsson, A.; Jonsson, H. *Comput. Mater. Sci.* **2006**, *36*, 354.
- (49) Sanville, E.; Kenny, S. D.; Smith, R.; Henkelman, G. *J. Comput. Chem.* **2007**, *28*, 899.
- (50) Kihlborg, L. *Ark. Kemi* **1963**, *21*, 357.
- (51) Cora, F.; Patel, A.; Harrison, N. M.; Roetti, C.; Catlow, C. R. A. *J. Mater. Chem.* **1997**, *7*, 959.
- (52) Sayede, A. D.; Amriou, T.; Pernisek, M.; Khelifa, B.; Mathieu, C. *Chem. Phys.* **2005**, *316*, 72.
- (53) Bouzidi, A.; Benramdane, N.; Tabet-Derranz, H.; Mathieu, C.; Khelifa, B.; Desfeux, R. *Mater. Sci. Eng. B* **2003**, *97*, 5.
- (54) Carter, E. A. *Science* **2008**, *321*, 800.
- (55) Anisimov, V. I.; Aryasetiawan, F.; Lichtenstein, A. I. *J. Phys.-Condes. Matter* **1997**, *9*, 767.
- (56) Bengone, O.; Alouani, M.; Blochl, P.; Hugel, J. *Phys. Rev. B* **2000**, *62*, 16392.
- (57) Wang, L.; Maxisch, T.; Ceder, G. *Phys. Rev. B* **2006**, *73*, 195107.
- (58) Solovvey, I. V.; Dederichs, P. H.; Anisimov, V. I. *Phys. Rev. B* **1994**, *50*, 16861.
- (59) Adams, S. *J. Solid State Chem.* **2000**, *149*, 75.
- (60) Braida, B.; Adams, S.; Canadell, E. *Chem. Mater.* **2005**, *17*, 5957.
- (61) Eda, K.; Sotani, N.; Kunitomo, M.; Kaburagi, M. *J. Solid State Chem.* **1998**, *141*, 255.

JP9017212